Priority Report

Cancer Research

# UV-Associated Mutations Underlie the Etiology of MCV-Negative Merkel Cell Carcinomas

Stephen Q. Wong[1], Kelly Waldeck[1], Ismael A. Vergara[1], Jan Schröder[1,2,3], Jason Madore[4], James S. Wilmott[4], Andrew J. Colebatch[1,5], Ricardo De Paoli-Iseppi[4], Jason Li[1], Richard Lupat[1], Timothy Semple[1], Gisela Mir Arnau[1], Andrew Fellowes[1], J. Helen Leonard[6], George Hruby[4], Graham J. Mann[4], John F. Thompson[4], Carleen Cullinane[1], Meredith Johnston[1], Mark Shackleton[1,7], Shahneen Sandhu[1,7], David D.L. Bowtell[1,5,7], Ricky W. Johnstone[1,7], Stephen B. Fox[1,5,7], Grant A. McArthur[1,7], Anthony T. Papenfuss[1,2,7,8], Richard A. Scolyer[4], Anthony J. Gill[9], Rodney J. Hicks[1,7], and Richard W. Tothill[1,5]

## Abstract

Merkel cell carcinoma (MCC) is an uncommon, but highly malignant, cutaneous tumor. Merkel cell polyoma virus (MCV) has been implicated in a majority of MCC tumors; however, viral-negative tumors have been reported to be more prevalent in some geographic regions subject to high sun exposure. While the impact of MCV and viral T-antigens on MCC development has been extensively investigated, little is known about the etiology of viral-negative tumors. We performed targeted capture and massively parallel DNA sequencing of 619 cancer genes to compare the gene mutations and copy number alterations in MCV-positive ($n = 13$) and -negative ($n = 21$) MCC tumors and cell lines. We found that MCV-positive tumors displayed very low mutation rates, but MCV-negative tumors exhibited a high mutation burden associated with a UV-induced DNA damage signature. All viral-negative tumors harbored mutations in *RB1*, *TP53*, and a high frequency of mutations in *NOTCH1* and *FAT1*. Additional mutated or amplified cancer genes of potential clinical importance included PI3K (*PIK3CA*, *AKT1*, *PIK3CG*) and MAPK (*HRAS*, *NF1*) pathway members and the receptor tyrosine kinase *FGFR2*. Furthermore, looking ahead to potential therapeutic strategies encompassing immune checkpoint inhibitors such as anti-PD-L1, we also assessed the status of T-cell–infiltrating lymphocytes (TIL) and PD-L1 in MCC tumors. A subset of viral-negative tumors exhibited high TILs and PD-L1 expression, corresponding with the higher mutation load within these cancers. Taken together, this study provides new insights into the underlying biology of viral-negative MCC and paves the road for further investigation into new treatment opportunities. *Cancer Res; 75(24); 5228–34. ©2015 AACR.*



## Introduction

Merkel cell carcinoma (MCC) is a rare but aggressive cutaneous neuroendocrine tumor that occurs most commonly in the fair skinned, elderly, and males with additional risk factors including immunosuppression and excessive sun exposure (1). The Merkel cell polyoma virus (MCV) has been implicated in 80% of MCC cases in the United States and Europe; however, this can differ significantly in other geographic regions such as Australia, where a much lower association with viral infection has been reported (~25%; ref. 2). While the impact of MCV and viral T-antigens on MCC development has been extensively investigated (3), little is known of the etiology of viral-negative tumors.

MCC has propensity for early spread and recurrence and while surgery and radiotherapy can achieve high rates of locoregional control, chemotherapy rarely provides durable responses for distant metastatic disease (4). The deployment of improved targeted therapies is likely to be achieved through a better understanding of MCC biology. Therefore, by applying massively parallel sequencing (MPS), we have searched for cancer gene mutations and somatic copy number alterations (SCNA) within MCC tumors with the view to characterize the genetic landscape of MCC subtypes based on viral association. Furthermore, we have investigated the presence of T-cell infiltrates and PD-L1 expression in MCC tumors, providing a rationale for use of immune checkpoint inhibitors for the treatment of MCC tumors irrespective of viral status.

## Materials and Methods

### Tumors and cell lines

The discovery cohort consisted of fresh-frozen and archival formalin-fixed paraffin embedded (FFPE) tissue samples

[1]Peter MacCallum Cancer Centre, Melbourne, Victoria, Australia. [2]Walter Eliza Hall Institute, Melbourne, Victoria, Australia. [3]Department of Computing and Information Systems, University of Melbourne, Melbourne, Victoria, Australia. [4]Melanoma Institute Australia and the University of Sydney, Sydney, New South Wales, Australia. [5]Department of Pathology, University of Melbourne, Melbourne, Victoria, Australia. [6]QIMR Berghofer Medical Research Institute, Brisbane, Queensland, Australia. [7]The Sir Peter MacCallum Department of Oncology, University of Melbourne, Melbourne, Victoria, Australia. [8]Department of Medical Biology, University of Melbourne, Melbourne, Victoria, Australia. [9]Cancer Diagnosis and Pathology Research Group Kolling Institute of Medical Research, University of Sydney, Sydney, New South Wales, Australia.

**Note:** Supplementary data for this article are available at Cancer Research Online (http://cancerres.aacrjournals.org/).

**Corresponding Author:** Richard W. Tothill, Peter MacCallum Cancer Centre, St Andrews Place, East Melbourne, Victoria 3002, Australia. Phone: 61-3-9656-1752; Fax: 61-3-9656-1414; E-mail: richard.tothill@petermac.org

**doi:** 10.1158/0008-5472.CAN-15-1877

representing primary and secondary tumors collected from the Peter MacCallum Cancer Centre ($n = 10$), Victorian Cancer Biobank ($n = 8$), Melanoma Institute Australia Biospecimen Bank ($n = 10$), Royal North Shore Hospital ($n = 2$), and the Cancer 2015 project ($n = 1$). Matched patient blood or tissue was available for eight patients. Cell lines MCC13 and MCC14 with matching immortalised normal blood lymphocytes were kindly provided by Nick Hayward (QIMR, Queensland, Australia). DNA sequencing of matching lymphocytic DNA confirmed the tumor cell line identity by genotype. MCC26 cells were purchased from Cell Bank Australia and were passaged for less than 6 months from receipt (Supplementary Table S1 for all clinicopathologic details of tumors and cell lines). An extended validation cohort of archival FFPE samples was collected from the Peter MacCallum Cancer Centre ($n = 13$) and the Royal North Shore Hospital ($n = 31$; Supplementary Table S2). All diagnoses were verified by histologic review and each MCC contained $\geq$70% tumor tissue. Biospecimens and clinical data were collected under institutional board approval according to the guidelines of the Australian National Health and Medical Research Council.

### DNA extraction

Genomic DNA from fresh tissue and blood was extracted using a QIAamp DNA Blood Mini Kit (Qiagen) according to the manufacturer's protocol. For archival FFPE samples, a modified protocol was used where tissue was digested in Buffer ATL (Qiagen) containing proteinase K at 56°C for 3 days with daily proteinase K replacement. Purified DNA was quantified using a fluorometric assay (Life Technologies).

### MCV droplet digital PCR

Viral status and copy number were determined by digital droplet PCR (ddPCR). Primer and probe sequences targeting MCV have been previously described (5). ddPCR reactions (25 μL) contained final concentrations of 1× ddPCR supermix for probes (without dUTP; Bio-Rad), 0.9 μmol/L each primer and 0.25 μmol/L of probe and between 1 to 5 ng of genomic DNA. Droplet generation and droplet reading for ddPCR was performed according to the manufacturer's instructions using Bio-Rad reagents on a QX200 AutoDG Droplet Digital PCR System and a QX200 Droplet Reader. The thermal cycling profile was 95°C: for 10 minutes followed by 40 cycles of 95°C for 15 seconds and 60°C for a minute. MCV copies were normalized to an ultra-conserved region of the genome located on chromosome 11q-14.1. Primers for this region were UC-chr11 Forward 5′- GGTTTCCTG-CTCACTCTGCTC-3′, UC-chr11 Reverse 5′- TCCACTTGCGTCAC-TACAGCTC-3′, with a product size of 202 bp. ddPCR reactions (25 μL) for this amplicon contained final concentrations of 1× ddPCR Evagreen mix (Bio-Rad), 0.9 μmol/L each primer the same aliquot of genomic DNA used for MCV testing. Thermal cycling profile was identical to that used for MCV detection.

### Targeted DNA capture and sequencing

A pan-cancer gene panel of 619 genes was manually curated from the literature and commercial cancer gene panels (Supplementary Methods and Supplementary Table S3). Exon co-ordinates were based on NCBI reference sequence database (HG19). Capture baits were designed to the MCV genome NCBI Accession NC_010277.1. The custom bait library was designed using Nimbledesign software (Nimblegen, Roche). Between 300 ng and 1 μg of input DNA was fragmented using a Covaris S2 sonicator (Covaris). Fragment libraries were prepared using the KAPA hyper prep kit using standard protocols (KAPA Biosystems). Hybridization capture was performed according to manufacturer's protocols (Nimblegen, Roche). Ten indexed sample libraries were run per lane on an Illumina HiSeq2500 platform (paired-end 100 bp) according to standard protocol. Performance metrics for samples are shown in Supplementary Table S4. Bioinformatic methods for sequence alignment and mutation detection have been previously described (6). To detect the insertion site of the virus, Socrates was used to predict fusions on the aligned capture data (7). Further detailed bioinformatics methods for variant detection, variant filtering, and viral integration detection are described in Supplementary Methods.

### Variant validation and *TERT* promoter sequencing

Mutations were validated using a combination of Sanger sequencing, high resolution melt analysis, or amplicon-based massively parallel sequencing. Mutations in the *TERT* promoter region were screened using amplicon-based massively parallel sequencing. Refer to Supplementary Methods and Supplementary Table S5 for detailed protocols and primer sequences.

### Low coverage whole-genome sequencing

Precapture fragmented libraries prepared for targeted sequencing were used for low-coverage WGS. Indexed libraries were normalized, pooled, and run on an Illumina Nextseq platform (paired-end 75 bp) according to the standard protocol. Performance metrics for samples are shown in Supplementary Table S4. Copy number calling was performed on the low-coverage whole-genome sequencing data using ControlFreec (version 6.7; ref. 8). Detailed bioinformatic methods for copy number detection and data filtering can be found in Supplementary Methods.

### Mutation signature clustering

Variants for each tumor were tallied relative to the 96 possible base substitutions considering the base changed, preceding, and trailing base. Gene Cluster 3.0 was then used to cluster samples by average linkage-centered clustering. Cluster diagrams and heatmaps were visualized and then exported from Treeview v1.1.6r2. Samples with less than 20 mutations were removed from clustering analysis.

### Immunohistochemistry

Four micron sections were cut, dewaxed in xylene, and rehydrated through a graded ethanol series. Appropriate control tissues were used on each individual slide to verify the quality of each stain. For NOTCH1, slides were pretreated with high pH target retrieval solution (Dako), and stained with NOTCH1 antibody (1:100, clone D1E11, Cell Signaling Technology, #3608) for 2 hours at 25°C. The slides were then incubated with the appropriate secondary antibody, followed by DAB Chromogen reagent (Dako), and counterstained with hematoxylin. Nuclear staining of NOTCH1 was scored semiquantitatively by a pathologist (A.J. Colebatch) by evaluating the predominant intensity of staining (0, 1, 2, or 3) and the proportion as a percentage of cells with that staining. An H-score was derived by multiplying intensity by the percentage of positive cells. Immunohistochemistry for CD3 and CD8 was performed on a Ventana Benchmark Ultra automated immunostainer (Ventana Medical Systems). Heat pretreatment

was performed using CC1solution (Ventana Medical Systems) for 64 minutes. Slides were incubated in CD3 antibody (1:100, clone SP7; Spring Bioscience) and CD8 antibody (1:100, clone 4B11; Leica) at 25°C for 30 to 60 minutes. Detection was achieved using the optiView universal DAB detection system (Ventana Medical Systems). CD3 and CD8 were scored semiquantitatively by a pathologist (A.J. Gill) by evaluating the predominant intensity of staining (0, 1, 2, or 3) for both the stroma and tumor-infiltrating lymphocytes and then combining scores into a single grade score (0–6). Immunochemistry for PD-L1 was performed on a Dako autostainer/PT-Link using the MACH3 Rabbit HRP Polymer Detection System (Biocare; M3R531) with high pH target retrieval buffer (Dako) as per manufacturer's instructions. Slides were incubated for 60 minutes at 25°C in the primary antibody against PD-L1 (1:500, E1L3N-XP-Rb mAb; CST#13684). PD-L1 was scored as previously described (9). Statistical analysis of immunohistochemical scoring was performed using GraphPad Prism Version 6.01 software and images were captured on a BX-61 Olympus microscope at ×10 magnification. Immunohistochemical scores are detailed in Supplementary Table S6.

### Western blot analysis

MCC13, MCC14, and MCC26 cell pellets were lysed into RIPA buffer (containing protease and phosphatase inhibitors) and then separated by SDS-PAGE. Western blotting was performed with anti-actin (1:10,000, MP Biomedicals #69100), phospho-ERK (1:1,000, Cell Signaling Technology #9101), ERK1/2 (1:1,000, Cell Signaling Technology #9102), and Notch1 (1:1,000, Cell Signaling Technology #3608) antibodies. Immunoreactive proteins were visualized on X-ray film using ECL reagents (Amersham).

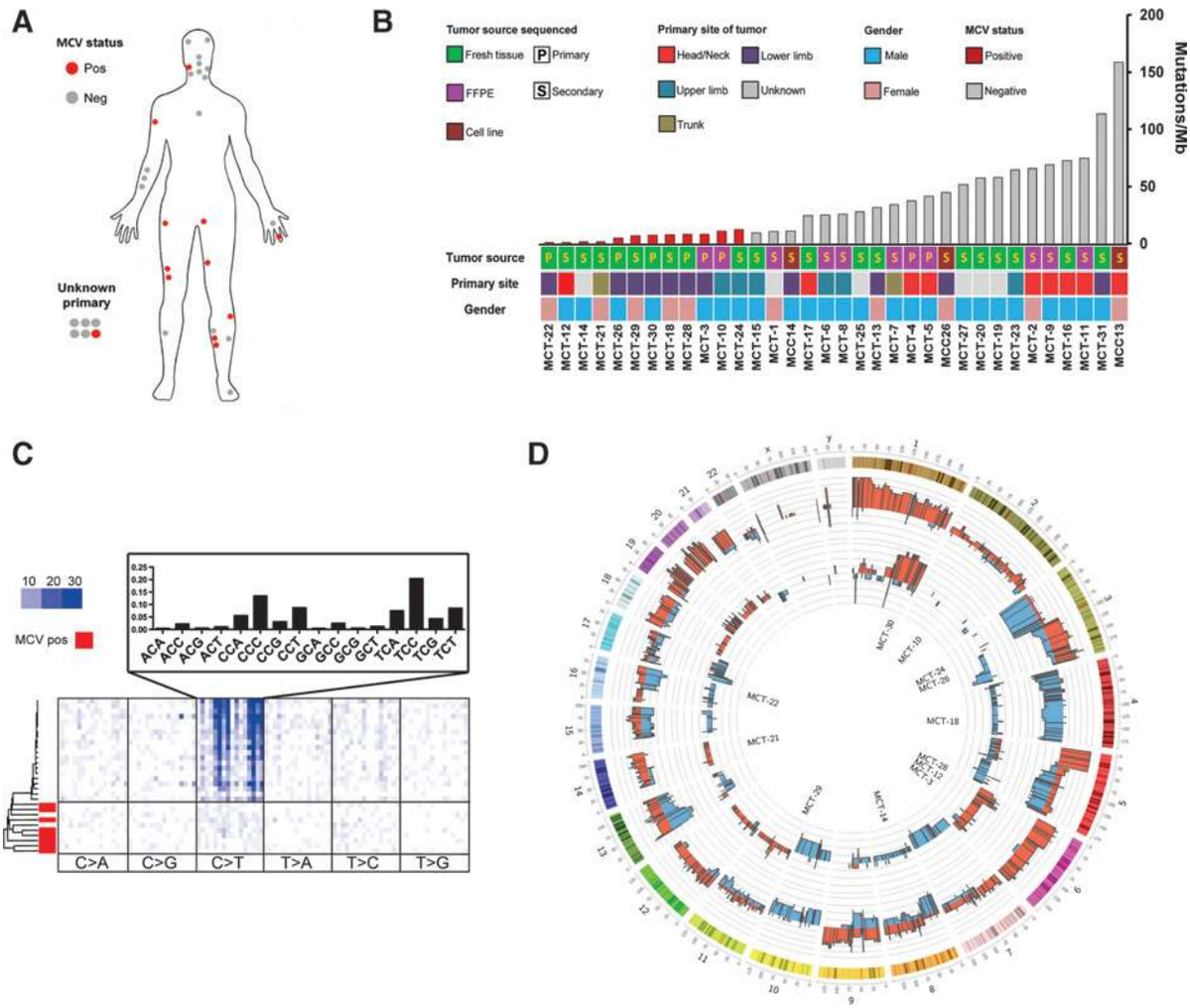


**Figure 1.**
Genomic landscape of MCC. A, primary site of MCC origin in the discovery cohort. B, mutational frequency (mutations per megabase) with corresponding clinicopathologic data and sequenced sample features. C, hierarchical clustering of samples and heatmap based on variant counts within 96 possible base substitutions as described by Alexandrov and colleagues (7). Histogram plot shows the arrayed order of base substitutions within heat map and the average frequency of C>T base substitutions for clustered tumors. UV signature indicated by high frequency of C>T transitions frequently at dipymidine sites. D, overall frequency of copy number alterations by genome position observed within $V^{-}MCC$ tumors (outer circle) and $V^{+}MCC$ (inner circle). Red, gains; blue, loss; scale in 10% increments of total. Three tumors were removed from SCNA analysis owing to poor quality data. Genomic integration sites in $V^{+}MCC$ tumors are indicated by sample name.

## Results and Discussion

We performed hybridization targeted capture and MPS of 619 curated cancer genes of interest, comparing the mutational spectrum of 12 viral-positive ($V^+MCC$) tumors, 19 viral-negative ($V^-MCC$) tumors, and three $V^-MCC$ cell lines. Somatic mutations were identified by referencing matched normal DNA and/or removing polymorphisms found in a compendium of unrelated germline DNA samples for cases where no matching normal blood or tissue was available (Supplementary Table S7). Variants of interest detected by targeted resequencing were further validated using orthogonal genotyping methods (Supplementary Table S5). Furthermore, we performed targeted amplicon-based DNA sequencing of the *TERT* promoter and validated selected cancer gene mutations of interest in an independent patient cohort ($n = 44$) (Supplementary Tables S2).

Most $V^-MCC$ tumors originated from sun-exposed regions of the head, neck, or limbs (Fig. 1A) and predominantly displayed a high mutation burden (Fig. 1B). Clustering analysis based on mutation counts within the context of 96 possible base substitutions showed that all but two $V^-MCC$ tumors clustered tightly as a group and harbored a distinctive UV signature as observed in other skin cancers (Fig. 1C; ref. 10). Conversely, all $V^+MCC$ tumors displayed low mutation counts and lacked the UV mutation signature including those that originated from presumed sun-exposed areas, such as the face and lower leg. This suggests that the mutagenic effects of sun damage had not significantly contributed to disease pathogenesis in the $V^+MCC$ group.

Using precapture DNA-sequencing libraries, we performed low coverage (1–3-fold) whole-genome sequencing to detect SCNAs by read depth analysis (Fig. 1D; Supplementary Tables S8 and S9). $V^-MCC$ tumors typically displayed a significantly greater degree of genomic instability (measured as a percentage of genome altered) compared with $V^+MCC$ (Mann–Whitney $U$ test, $P = 0.002$). Some differences in the frequency (>20%) of large chromosomal SCNAs could be observed between subtypes (e.g., gain chr1p, chr3q, chr5p, chr9, chr20p and loss chr3p, chr4, 13q in $V^-MCC$; loss of 17p *in* $V^+MCC$), while other SCNAs appeared to be shared with a frequency greater than 10% in both groups (gain chr1q, 6q, chr9, 19q, 20q and loss chr5q, chr10). Sequence capture of MCV DNA enabled mapping of viral integration sites

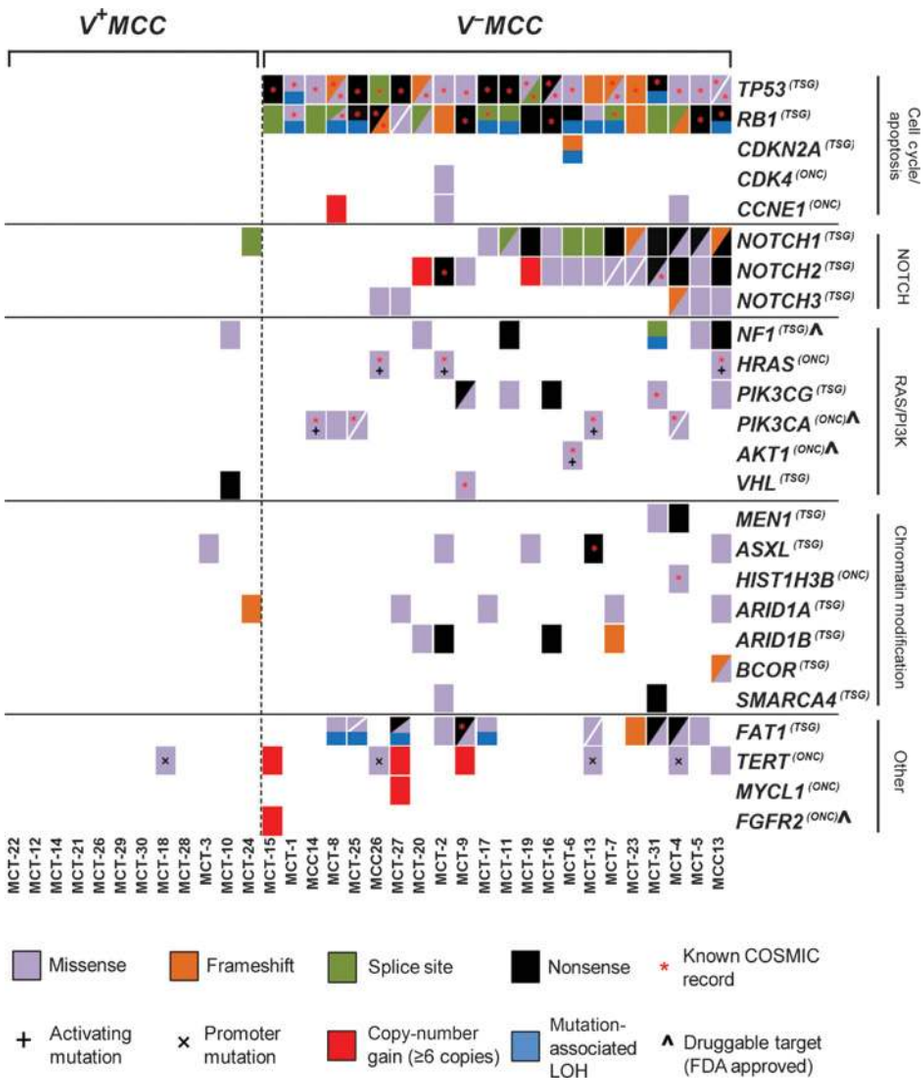


**Figure 2.**
Cancer genes affected by mutation or copy number alterations. Samples are grouped on the basis of their MCV status and ranked on the prevalence of commonly mutated genes *TP53*, *RB1*, *NOTCH1*, *NOTCH2*, and *NOTCH3*. Genes are grouped together on their respectively core function/pathway as shown on the right. ONC, oncogene; TSG, tumor suppressor gene; LOH, loss of heterozygosity. *TERT* promoter mutations included chromosomal positions 124 and 146 bp upstream of the *TERT* translational start site as detailed in Supplementary Methods.

and digital droplet PCR was used to enumerate between 1 and 6 viral copies per tumor. No known cancer genes were found proximal (<1 Mb) to viral integrations (Supplementary Table S10). Intriguingly, we observed focal SCNAs in close proximity to viral insertions, suggesting localized genomic instability may have occurred early in the ancestral clone (Supplementary Fig. S1).

Given the high rate of UV-induced DNA damage we stringently interpreted the mutation and SCNA data to focus on known cancer genes and pathways (Fig. 2). Consistent with a prior report, disruptive *RB1* mutations could be detected in all *V*$^{-}$*MCC* (11). Ubiquitous *TP53* mutations were also specific to *V*$^{-}$*MCC*. Pathogenic mutations and high-level amplification events affecting other cell-cycle regulators (*CDKN2A*, *CCNE1*, *CDK4*) were also detected, which was unexpected given these genes lie directly upstream of p53 and RB1 in respective signaling pathways.

Novel, high-frequency *NOTCH* mutations were detected in *V*$^{-}$*MCC* tumors. *NOTCH1*-mutant tumors and cell lines displayed low or absent nuclear NOTCH1 protein expression, supporting a likely tumor-suppressor function in MCC (Fig. 3A–D; Supplementary Table S6). A high frequency of protein truncating mutations were also found in the cadherin *FAT1*. Other mutated genes included chromatin modifiers (e.g., *ARID1A*, *CREBBP*, *MEN1*, *BCOR*, *ASXL1*), the histone *HIST1H3B* and the HIF regulatory protein *VHL*. Consistent with prior reports, a high-level amplification of the transcription factor *MYCL1* was identified in one case (12). Furthermore, genome amplification and/or promoter mutations of the telomerase subunit *TERT* were observed with high-level amplification occurring specifically within *V*$^{-}$*MCC* tumors.

Mutations in genes representing potential therapeutic targets were identified in a substantial number of *V*$^{-}$*MCC* tumors. *HRAS* mutations were found in a single *V*$^{-}$*MCC* tumor from the discovery cohort, one from the extended validation cohort and two *V*$^{-}$*MCC* cell lines (combined *V*$^{-}$*MCC* frequency 4/60; Supplementary Table S2). *HRAS*-mutant cells lines expressed elevated phosphorylated ERK (Supplementary Fig. S2); however, these lines were resistant to MEK inhibition, suggesting limited translational potential as a single agent in these patients (Supplementary Table S11). *NF1* mutations were also identified in some *V*$^{-}$*MCC* and may represent a potential alternative mechanism to RAS pathway dysregulation. Consistent with prior studies, activating *PIK3CA* mutations were present in *V*$^{-}$*MCC* from the discovery and validation cohorts (combined *V*$^{-}$*MCC*, frequency 11/60; refs. 13, 14). Furthermore, we identified an oncogenic *AKT1*$^{E17K}$ mutation in one tumor and missense/nonsense mutations in *PIK3CG*, extending the known spectrum of mutations in the PI3K pathway. Finally, a high-level amplification of the receptor tyrosine kinase *FGFR2* was also observed in one case offering yet another potential therapeutic target.

Cancers with high mutation burden, including those associated with chronic UV exposure, frequently display elevated adaptive immune response, and show durable responses to immune checkpoint inhibition therapy (15, 16). To investigate this within MCC, we scored all tumors in the discovery cohort for the presence of T-cell infiltrating lymphocytes (TIL) and assessed the expression of the PD-L1 ligand (combined% positive tumor and macrophage cells) as a marker of immune checkpoint response (Fig. 4A; Supplementary Table S6). Consistent with their viral etiology and a previous study, *V*$^{+}$*MCC* generally had high TIL grade and PD-L1 levels (Fig. 4B and C and Supplementary Fig. S3) (17). However, we also noted a spectrum of low to high TIL grades and PD-L1 expression in *V*$^{-}$*MCC*, which is a novel observation within this group. Within the *V*$^{-}$*MCC* group, PD-L1–positive tumors (>1% positive) had significantly higher mutation burden compared with PD-L1–negative tumors (Fig. 4D). This may reflect an increased likelihood of neoantigen presentation in heavily mutated cancers.

In summary, our findings support the paradigm of two distinct disease etiologies for MCC: one driven by MCV integration and

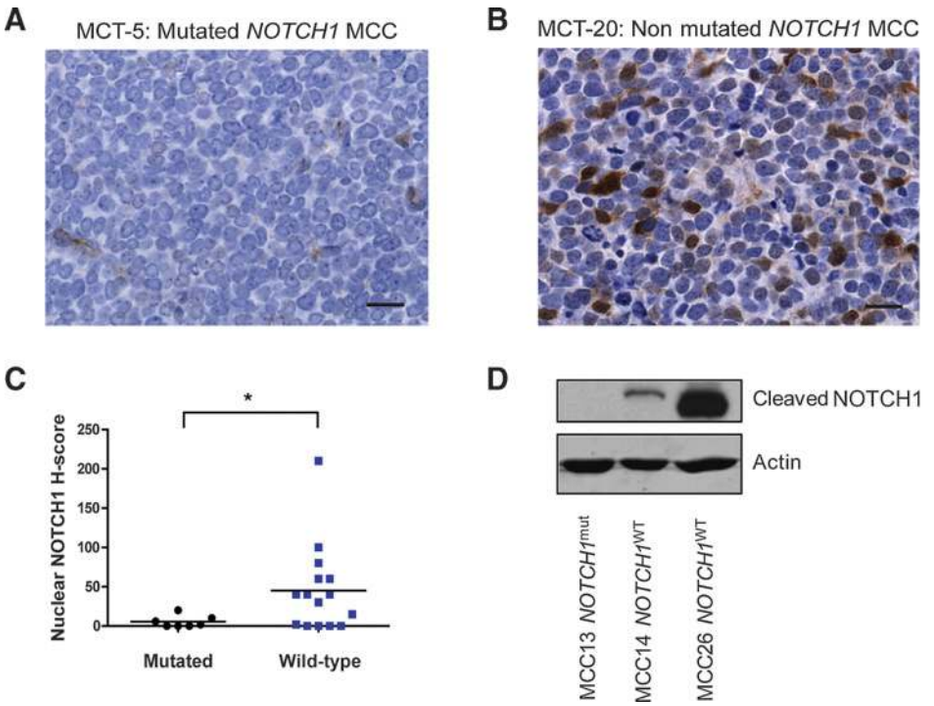


**Figure 3.**
*NOTCH1* mutations associated with loss of NOTCH1 protein expression in MCC tumors. Representative micrographs of NOTCH1 protein expression by immunohistochemistry in MCC with mutant (A) and wild-type (B) *NOTCH1* (objective lens 40×; scale bars, 20 μm). C, nuclear NOTCH1 H-scores plotted between NOTCH1-mutated versus nonmutated MCC tumors. Singular values with median line are shown. *, $P = 0.0312$, Mann–Whitney *U* test. D, Western blot analysis of cleaved NOTCH1 protein expression in the Merkel cell carcinoma lines MCC13, MCC14, and MCC26. NOTCH1$^{mut}$, mutated *NOTCH1* gene; NOTCH1$^{WT}$, nonmutated *NOTCH1* gene.

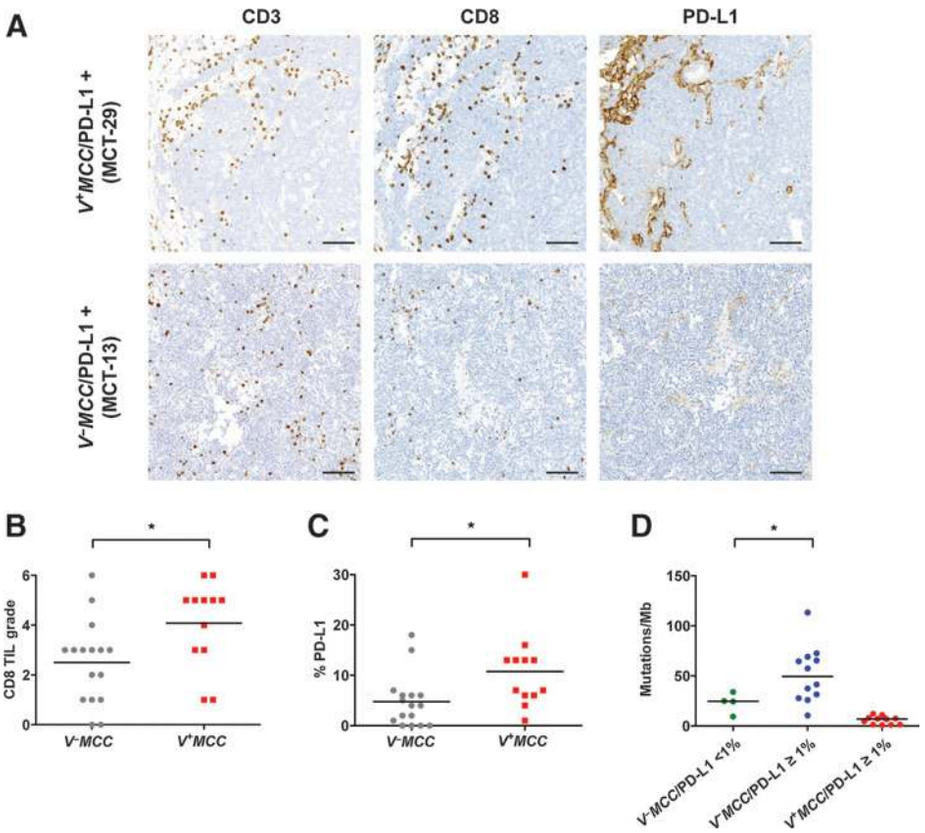


**Figure 4.**
Immune response and correlation to mutation burden. A, representative micrographs of CD3, CD8, and PD-L1 protein expression assessed by immunohistochemistry in one $V^-$MCC and one $V^+$MCC (objective lens 10×; scale bars, 100 μm). B, combined peritumoral (1–3) and tumoral (1–3) $CD8^+$ T-cell scores in V-MCC and $V^+$MCC. C, PD-L1 expression (percentage of cells stained) between $V^-$MCC and $V^+$MCC. D, mutation frequency in MCCs grouped on the basis of MCV status and cells < or ≥1% staining for PD-L1. All plots show singular values with median line. *, $P < 0.05$, Mann–Whitney *U* test.

seemingly requiring few additional mutations, and the other driven by UV-associated activating and tumor-suppressing mutations. Merkel cells are thought to arise from epidermal stem cells, which can also give rise to keratinocytes (18). It is therefore interesting that *$V^-$MCC* exhibit genetic similarities to squamous cell carcinoma (19) and sun-damaged skin (20), including a UV mutation profile and recurrent mutations in *NOTCH1*, *TP53*, *FAT1*, and *HRAS*. Meanwhile, disruption of RB1 is clearly a required event in all MCC tumors, either through mutation or sequestration by the viral T-antigen, and is a distinguishing feature from other nonmelanoma skin cancers. Importantly, we have shown that *$V^-$MCC* harbor mutations and gene amplifications that may direct therapeutic intervention, providing a rationale for clinical sequencing in this group. In addition, our findings suggest that similar to sun-exposed and heavily mutated melanoma, a proportion of *$V^-$MCC* patients may benefit from immune checkpoint blockade therapy.

## Disclosure of Potential Conflicts of Interest

R.W. Johnstone has received speakers bureau honoraria from and is a consultant/advisory board member for Novartis. G.A McArthur reports receiving commercial research grant from Celgene, Novartis, and Ventana and is a consultant/advisory board member for Provectus. No potential conflicts of interest were disclosed by the other authors.

## Authors' Contributions

**Conception and design:** S.Q. Wong, C. Cullinane, M. Shackleton, G.A. McArthur, A.T. Papenfuss, R.A. Scolyer, A.J. Gill, R.J. Hicks, R.W. Tothill
**Development of methodology:** S.Q. Wong, K. Waldeck, J. Li, T. Semple, A. Fellowes, S. Sandhu, G.A. McArthur, A.T. Papenfuss, A.J. Gill, R.W. Tothill
**Acquisition of data (provided animals, acquired and managed patients, provided facilities, etc.):** S.Q. Wong, K. Waldeck, J. Madore, J.S. Wilmott, A.J. Colebatch, R. De Paoli-Iseppi, T. Semple, G.M. Arnau, A. Fellowes, J.H. Leonard, G. Hruby, G.J. Mann, M. Johnston, M. Shackleton, S. Sandhu, S.B. Fox, A.J. Gill, R.J. Hicks
**Analysis and interpretation of data (e.g., statistical analysis, biostatistics, computational analysis):** S.Q. Wong, K. Waldeck, I.A. Vergara, J. Schröder, J.S. Wilmott, J. Li, R. Lupat, C. Cullinane, D.D.L. Bowtell, A.T. Papenfuss, R.A. Scolyer, A.J. Gill, R.J. Hicks, R.W. Tothill
**Writing, review, and/or revision of the manuscript:** S.Q. Wong, K. Waldeck, J. Schröder, J.S. Wilmott, A.J. Colebatch, R. De Paoli-Iseppi, J. Li, G. Hruby, G.J. Mann, J.F. Thompson, C. Cullinane, M. Johnston, S. Sandhu, D.D.L. Bowtell, R.W. Johnstone, S.B. Fox, G.A. McArthur, A.T. Papenfuss, R.A. Scolyer, A.J. Gill, R.J. Hicks, R.W. Tothill
**Administrative, technical, or material support (i.e., reporting or organizing data, constructing databases):** S.Q. Wong, J.S. Wilmott, J. Li, A.J. Gill
**Study supervision:** C. Cullinane, A.J. Gill, R.J. Hicks, R.W. Tothill

## Acknowledgments

The authors thank John Parisot and the Cancer 2015 study, David Gyorki, Jeanette Raleigh, Annette Hogg, and Anatomical Pathology at Peter MacCallum Cancer Centre, Nicholas Hayward and Lauren Aoude of the QIMR Berghofer Medical Research Institute, colleagues at Melanoma Institute Australia and Royal Prince Alfred Hospital, Sydney, Australia, and the Victorian Cancer Biobank for their contributions to the study.

## Grant Support

This work was supported by generous funding from the Peter MacCallum Cancer Foundation and the National Health and Medical Research Council.

Received July 13, 2015; revised September 10, 2015; accepted October 1, 2015; published OnlineFirst December 1, 2015.

## References


1. Albores-Saavedra J, Batich K, Chable-Montero F, Sagy N, Schwartz AM, Henson DE. Merkel cell carcinoma demographics, morphology, and survival based on 3870 cases: a population based study. J Cutan Pathol 2010;37:20–7.
2. Paik JY, Hall G, Clarkson A, Lee L, Toon C, Colebatch A, et al. Immunohistochemistry for Merkel cell polyomavirus is highly specific but not sensitive for the diagnosis of Merkel cell carcinoma in the Australian population. Hum Pathol 2011;42:1385–90.
3. Chang Y, Moore PS. Merkel cell carcinoma: a virus-induced human cancer. Annu Rev Pathol 2012;7:123–44.
4. Ramahi E, Choi J, Fuller CD, Eng TY. Merkel cell carcinoma. Am J Clin Oncol 2013;36:299–309.
5. Becker JC, Schrama D, Houben R. Merkel cell carcinoma. Cell Mol Life Sci 2009;66:1–8.
6. Tothill RW, Li J, Mileshkin L, Doig K, Siganakis T, Cowin P, et al. Massively-parallel sequencing assists the diagnosis and guided treatment of cancers of unknown primary. J Pathol 2013;231:413–23.
7. Schroder J, Hsu A, Boyle SE, Macintyre G, Cmero M, Tothill RW, et al. Socrates: identification of genomic rearrangements in tumour genomes by re-aligning soft clipped reads. Bioinformatics. 2014 Jan 22. [Epub ahead of print].
8. Boeva V, Popova T, Bleakley K, Chiche P, Cappo J, Schleiermacher G, et al. Control-FREEC: a tool for assessing copy number and allelic content using next-generation sequencing data. Bioinformatics 2012;28:423–5.
9. Madore J, Vilain RE, Menzies AM, Kakavand H, Wilmott JS, Hyman J, et al. PD-L1 expression in melanoma shows marked heterogeneity within and between patients: implications for anti-PD-1/PD-L1 clinical trials. Pigment Cell Melanoma Res 2015;28:245–53.
10. Alexandrov LB, Nik-Zainal S, Wedge DC, Campbell PJ, Stratton MR. Deciphering signatures of mutational processes operative in human cancer. Cell Rep 2013;3:246–59.
11. Cimino PJ, Robirds DH, Tripp SR, Pfeifer JD, Abel HJ, Duncavage EJ. Retinoblastoma gene mutations detected by whole exome sequencing of Merkel cell carcinoma. Mod Pathol 2014;8:1073–87.
12. Paulson KG, Lemos BD, Feng B, Jaimes N, Peñas PF, Bi X, et al. Array-CGH reveals recurrent genomic changes in Merkel cell carcinoma including amplification of L-Myc. J Invest Dermatol 2009;129:1547–55.
13. Hafner C, Houben R, Baeurle A, Ritter C, Schrama D, Landthaler M, et al. Activation of the PI3K/AKT pathway in Merkel cell carcinoma. PLoS ONE 2012;7:e31255.
14. Nardi V, Song Y, Santamaria-Barria JA, Cosper AK, Lam Q, Faber AC, et al. Activation of PI3K signaling in Merkel cell carcinoma. Clin Cancer Res 2012;18:1227–36.
15. Topalian SL, Hodi FS, Brahmer JR, Gettinger SN, Smith DC, McDermott DF, et al. Safety, activity, and immune correlates of anti-PD-1 antibody in cancer. N Engl J Med 2012;366:2443–54.
16. Snyder A, Makarov V, Merghoub T, Yuan J, Zaretsky JM, Desrichard A, et al. Genetic basis for clinical response to CTLA-4 blockade in melanoma. N Engl J Med 2014;371:2189–99.
17. Lipson EJ, Vincent JG, Loyo M, Kagohara LT, Luber BS, Wang H, et al. PD-L1 expression in the Merkel cell carcinoma microenvironment: association with inflammation, Merkel cell polyomavirus and overall survival. Cancer Immunol Res 2013;1:54–63.
18. Morrison KM, Miesegaes GR, Lumpkin EA, Maricich SM. Mammalian Merkel cells are descended from the epidermal lineage. Dev Biol 2009;336:76–83.
19. South AP, Purdie KJ, Watt SA, Haldenby S, den Breems NY, Dimon M, et al. NOTCH1 mutations occur early during cutaneous squamous cell carcinogenesis. J Invest Dermatol 2014;134:2630–8.
20. Martincorena I, Roshan A, Gerstung M, Ellis P, Van Loo P, McLaren S, et al. Tumor evolution. High burden and pervasive positive selection of somatic mutations in normal human skin. Science 2015;348:880–6.